Science Advances
AAAS

Supplementary Materials for

Wafer-scale freestanding vanadium dioxide film

He Ma, Xiao Xiao, Yu Wang, Yufei Sun, Bolun Wang, Xinyu Gao, Enze Wang, Kaili Jiang, Kai Liu*, Xinping Zhang*

*Corresponding author. Email: liuk@tsinghua.edu.cn (K.L.); zhangxinping@bjut.edu.cn (X.Z.)

Published 8 December 2021, *Sci. Adv.* **7**, eabk3438 (2021)
DOI: 10.1126/sciadv.abk3438

This PDF file includes:

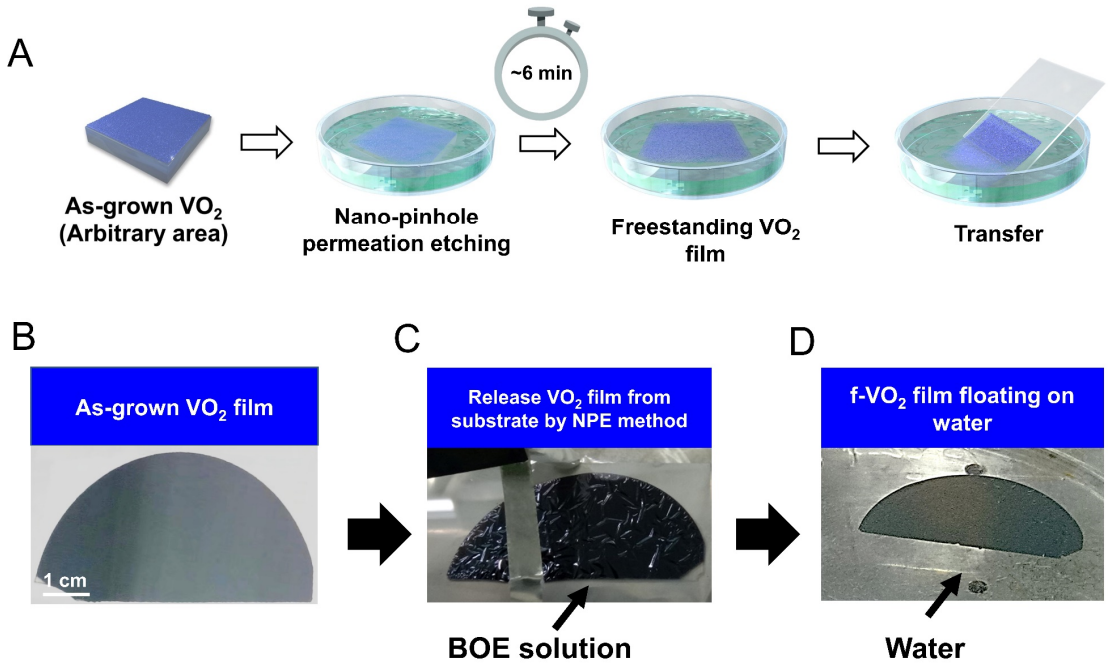

Fig. S1 Wafer-scale f-VO_2 film prepared by the nano-pinhole permeation-etching method. (**A**) Schematic diagram for preparing freestanding VO_2 (f-VO_2) films. (**B**) Optical image of as-grown VO_2 film on the quartz substrate. (**C**) Detachment of the VO_2 film by NPE method. (**D**) f-VO_2 film floating on water. Photo credit: He Ma, Beijing University of Technology.

Fig. S1A shows the schematic diagram for preparing the freestanding VO_2 (f-VO_2) film. The VO_2 film with nano-pinholes (Fig. S1B) was immersed into the BOE solution in a stainless-steel container. By removing the VO_2/SiO_2 interface layer, the VO_2 layer gradually separated from the SiO_2 substrate (Fig. S1C). After removing the interface layer, the container was slowly lifted from the BOE solution and gently immersed in clean water. The surface tension of the water caused the f-VO_2 film to float on the surface (Fig. S1D). We then transferred the floating f-VO_2 film to another dish with clean water to remove the residual BOE solution. Finally, we transferred the f-VO_2 film to the desired target substrate.

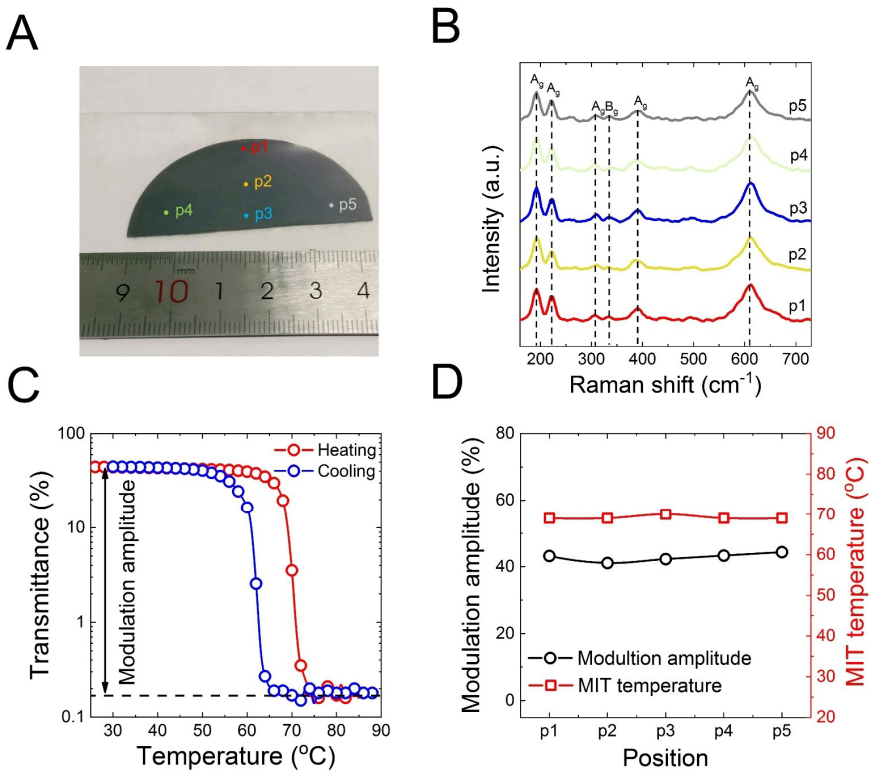

Fig. S2 Homogeneity of wafer-scale f-VO_2 film in its phase-transition and structural properties. (**A**) Optical image of the wafer-scale f-VO_2 film transferred to a polyethylene terephthalate (PET) substrate. Photo credit: He Ma, Beijing University of Technology. (**B**) Raman spectra of the f-VO_2/PET film at 5 positions (p1-p5, as labeled in S2A). (**C**) Temperature-dependent transmittance of the f-VO_2/PET film at the wavelength of 1600 nm. (**D**) Modulation amplitude and MIT temperature (extracted from the heating curves) of the f-VO_2/PET film at p1-p5.

We transferred a wafer-scale f-VO_2 film to a polyethylene terephthalate (PET) substrate to facilitate the characterization. Subsequently, the structural and the phase-transition homogeneity of the f-VO_2/PET film were evaluated by optical approaches. As shown in Figs. S2A and S2B, Raman spectra collected from 5 different positions (labeled as p1-p5 in Fig. S2A) in the f-VO_2/PET film identically reveal the VO_2 lattice vibration modes, demonstrating a good structural homogeneity of the wafer-scale f-VO_2 film. Moreover, the optical transmittance-temperature curves around the same 5 positions were also measured at the wavelength of 1600 nm, as shown in Figs. S2C and S2D. Due to the metal-insulator phase transition (MIT) of VO_2, the transmittance of the f-VO_2/PET film is modulated from 45% to 0.18% when the temperature is increased from 25 to 90 °C (Fig. S2C). The f-VO_2/PET film has almost identical MIT temperature and the modulation amplitude of the transmittance at the 5 different positions distributed in the entire film (Fig. S2D), indicating the excellent phase-transition homogeneity of the wafer-scale f-VO_2 film.

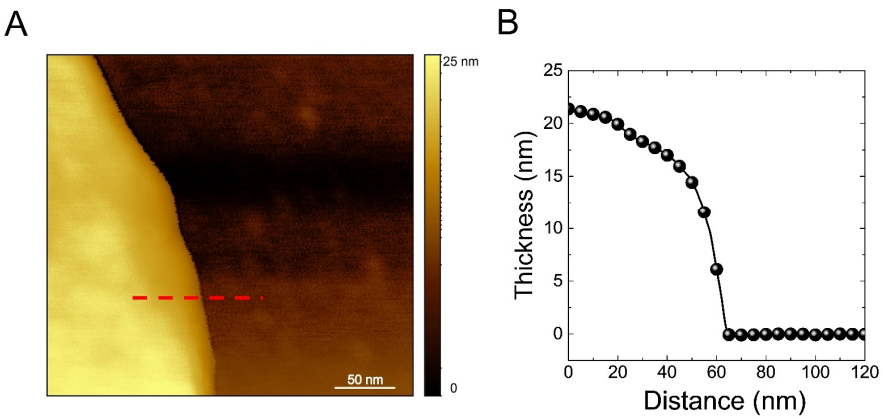

Fig. S3 Atomic force microscopy characterization of 20-nm-thick f-VO_2 film. (**A**) Atomic force microscopy (AFM) image of the f-VO_2 film. (**B**) Height profile of the along the dashed line in Fig. S3A, indicating the thickness of the f-VO_2 film was 20 nm.

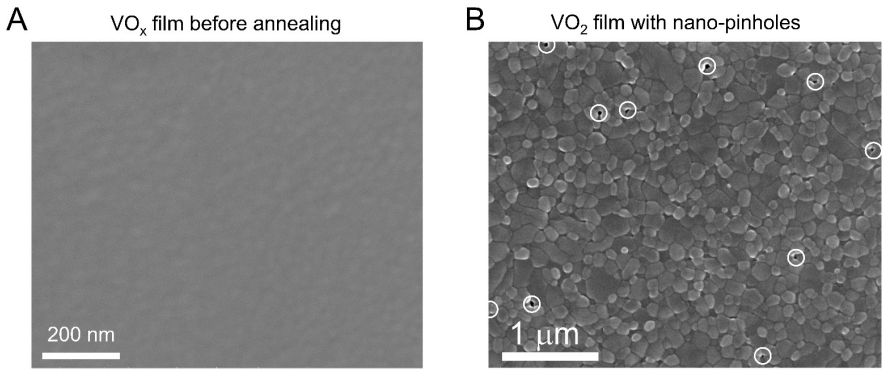

Fig. S4 Scanning electron microscopy characterizations of VO_2 film. (**A**) before annealing and (**B**) after annealing.

The VO_2 film used in this work was deposited on the SiO_2 substrate *via* reactive magnetic sputtering and a post-annealing process. The thickness of the VO_2 film was controlled *via* the sputtering time. We compared the surface morphology of the VO_2 film before and after the post-annealing process under a low-pressure oxygen atmosphere. The VO_x film was smooth and dense (Fig. S4A), which transformed to form a granulated VO_2 film because of crystallization of the VO_x film after annealing. From the scanning electron microscopy (SEM) images (Fig. S4B), numerous nano-pinholes are observed on the VO_2 film.

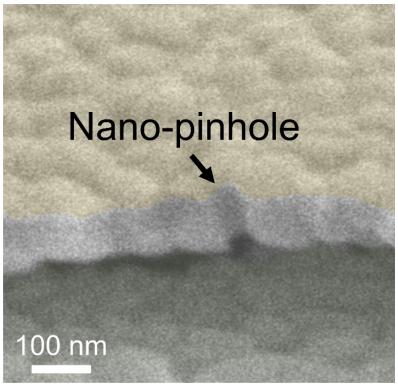

Fig. S5 SEM characterization of the cross-section of the f-VO_2 film. The nano-pinhole is indicated by the black arrow.

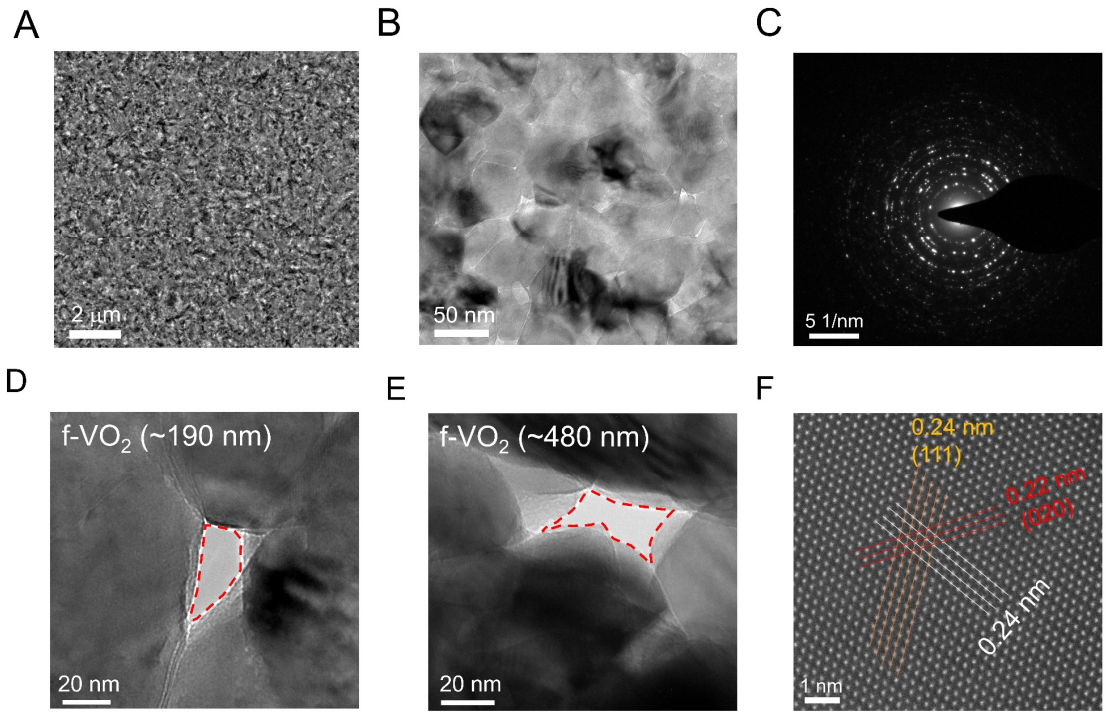

Fig. S6. Transmission electron microscopy characterization of the f-VO_2 film. (**A**) Transmission electron microscopy (TEM) image of the f-VO_2 film. (**B**) Enlarged TEM image of the f-VO_2 film. (**C**) Typical electron diffraction pattern of the f-VO_2 film. (**D**) Enlarged TEM image of a nano-pinhole in the 190-nm-thick f-VO_2 film. (**E**) Enlarged TEM image of a nano-pinhole in the 480-nm-thick f-VO_2 film. (**F**) Atomic high-angle annular dark-field scanning TEM image of a crystalline grain in f-VO_2 film.

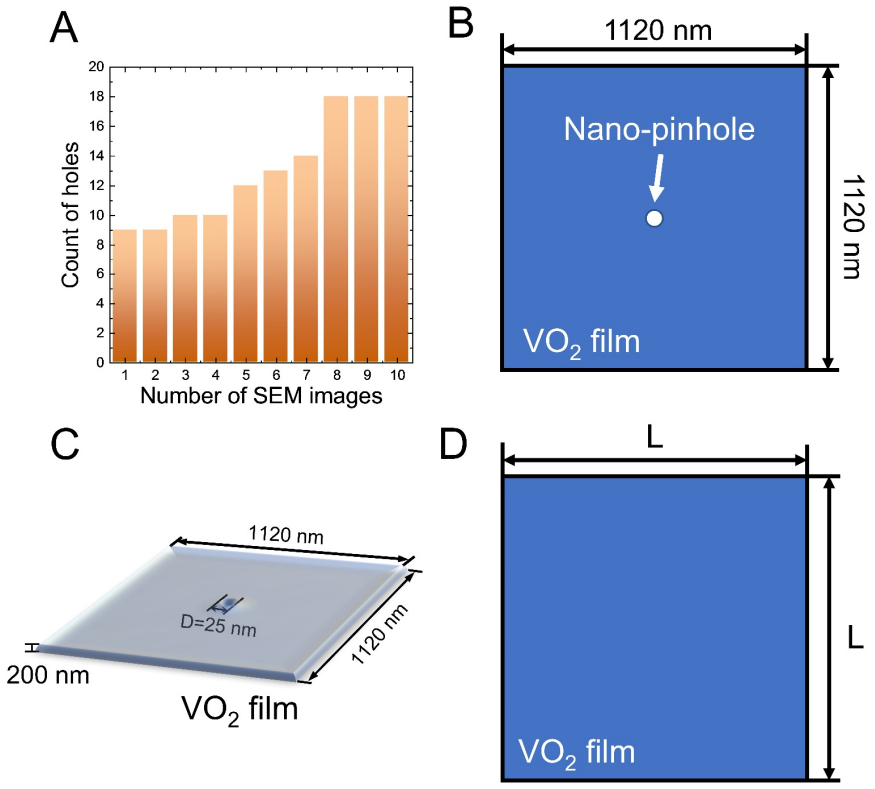

Fig. S7. Histogram of nano-pinholes in the VO_2 film and geometrical models. (**A**) Histogram of the number of nano-pinholes in the VO_2 film. (**B**) Geometrical model for releasing VO_2 film *via* NPE method. (**C**) Three-dimensional geometrical model of 200-nm-thick f-VO_2 film. (**D**) Geometrical model for the release of the dense VO_2 film *via* normal side etching.

The release time for the dense VO_2 film *via* normal side etching in Fig. 1F was calculated according to the geometrical model in Fig. S7D. The shape of the VO_2 film was simplified to a square. The etching rate of the BOE solution was 100 nm/min, and the release time was calculated by L/2/100.

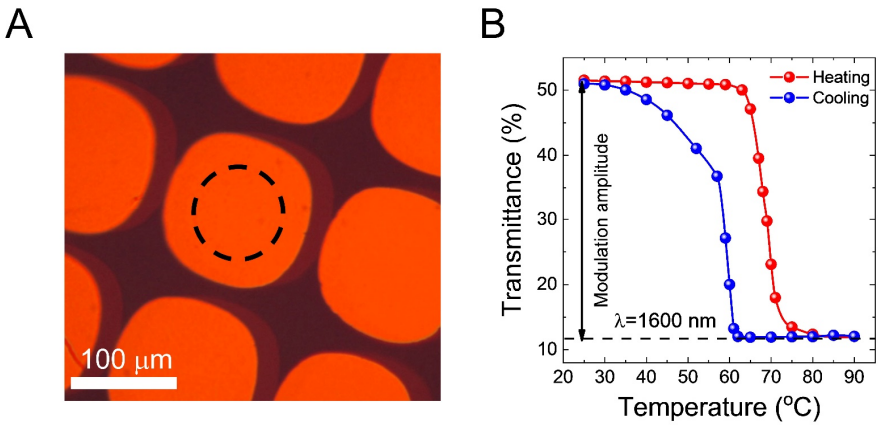

Fig. S8. Temperature-dependent transmittance of the f-VO_2 film suspended on a copper grid. (**A**) Optical microscopy image of the f-VO_2 film suspended on the copper grid. (**B**) Temperature-dependent transmittance of the f-VO_2 film marked by the cycle.

We measured the temperature-dependent transmittance (I) of a 90-nm-thick f-VO_2 film suspended on a copper grid (Fig. S8A) at the wavelength 1600 nm. The modulation amplitude is defined as $I_{(25\ ^{o}C)}$-$I_{(90\ ^{o}C)}$. Therefore, the modulation amplitude of the f-VO_2 film reaches ~ 39% (Fig. S8B).

Table S1 Comparison of the modulation amplitude at the wavelength of 1600 nm of VO_2 films prepared by various methods.

Sample	Thickness of VO_2 layer (nm)	Preparation method	Modulation amplitude at 1600 nm	References
VO_2/graphene/PET	40	Sputtering	33%	(*52*)
VO_2/glass	130	Physical vapor deposition	35%	(*53*)
VO_2/muscovite	50	Pulsed laser deposition	32%	(*54*)
VO_2/mica	40	Molecular beam epitaxy	28%	(*55*)
PI/Cr_2O_3/VO_2	80	Sputtering	33%	(*56*)
VO_2/SnO_2/glass	60	Pulsed laser deposition	35%	(*57*)
VO_2/Al_2O_3	50	Pulsed laser deposition	33%	(*58*)
VO_2/quartz	90	Pulsed laser deposition	36%	(*59*)
Epitaxial VO_2 on Al_2O_3	40	Sputtering	25%	(*60*)
Epitaxial VO_2 on c-plane sapphire	100	Pulsed laser deposition	20%	(*10*)
f-VO_2 film	**90**	**Sputtering**	**39%**	**This work**
f-VO_2 film	**190**	**Sputtering**	**49%**	**This work**
f-VO_2/mica film	**190**	**Sputtering**	**50%**	**This work**

Table S2 Comparison of the electrical property of the f-VO_2 film with other free-standing VO_2 films

Samples	Resistance change ratio across MIT ($R_{30\,^oC}$ /$R_{90\,^oC}$)	References
Epitaxial VO_2 membrane transferred onto PET	~ 2200	(*17*)
Small-scale freestanding VO_2 membrane	~ 300	(*61*)
Small-scale freestanding VO_2 membrane	~ 500	(*62*)
VO_2 membrane transferred onto glass	~ 600	(*18*)
Large-scale f-VO_2 films	**~ 2400**	**This work**

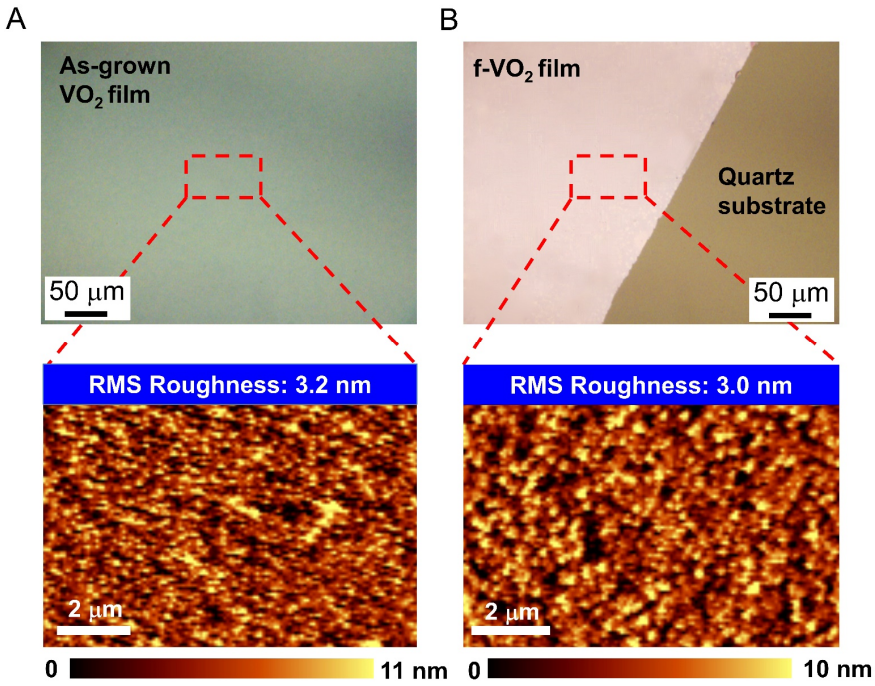

Fig. S9 Comparison of surface morphologies of as-grown VO_2 film and f-VO_2 film. (**A**) Optical microscopy image and AFM image of the as-grown VO_2 film . (**B**) Optical microscopy image and AFM image of the f-VO_2 film transferred to the quartz substrate.

The root-mean-square (RMS) roughness of our VO_2 films is calculated according to the equation $\sqrt{\frac{1}{M\times N}\Sigma_{j=1}^{N}\Sigma_{i=1}^{M}[z(x_i,y_j)-\bar{z}]^2}$ by the 'WITec Project' software, where M presents the number of pixels in a row, N presents the number of pixels in a column, x_i, y_j, and z present the coordinates in x axis, y axis, and the height, and $\bar{z}$ presents the mean height. The RMS roughnesses of the as-grown VO_2 film (thickness ~80 nm) and the f-VO_2 film (thickness ~80 nm) transferred to the quartz substrate are 3.2 and 3.0 nm, respectively. These values are comparable with the RMS roughness of the epitaxial VO_2 crystal film on sapphire, as reported in the literature(J. Appl. Phys., 2013, 113, 043707, Phys. Rev. Mater, 2018, 2, 034605).

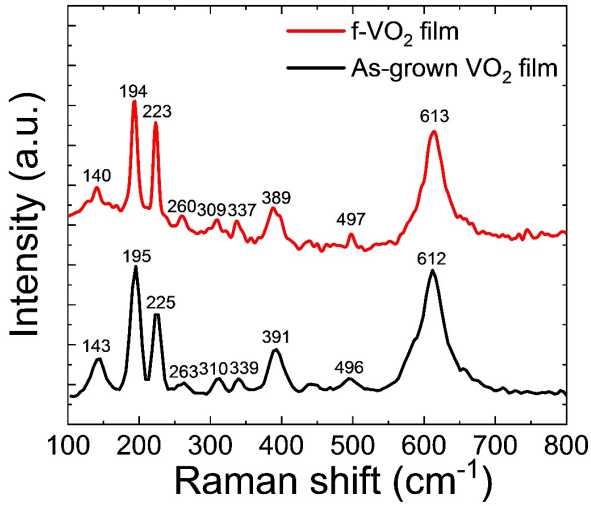

Fig. S10 Raman spectra of VO_2 films. The black line: as-grown VO_2 film. The red line: f-VO_2 film transferred to the quartz substrate.

Because of the small thermal capacity of the f-VO_2 film, the f-VO_2 film was easily heated by the laser. To decrease the thermal effect of laser in the Raman measurement, particularly in the temperature-dependent Raman measurement, we measured the Raman spectrum of the f-VO_2 film transferred to the quartz substrate and compared it with that of as-grown VO_2 film (Fig. S10).

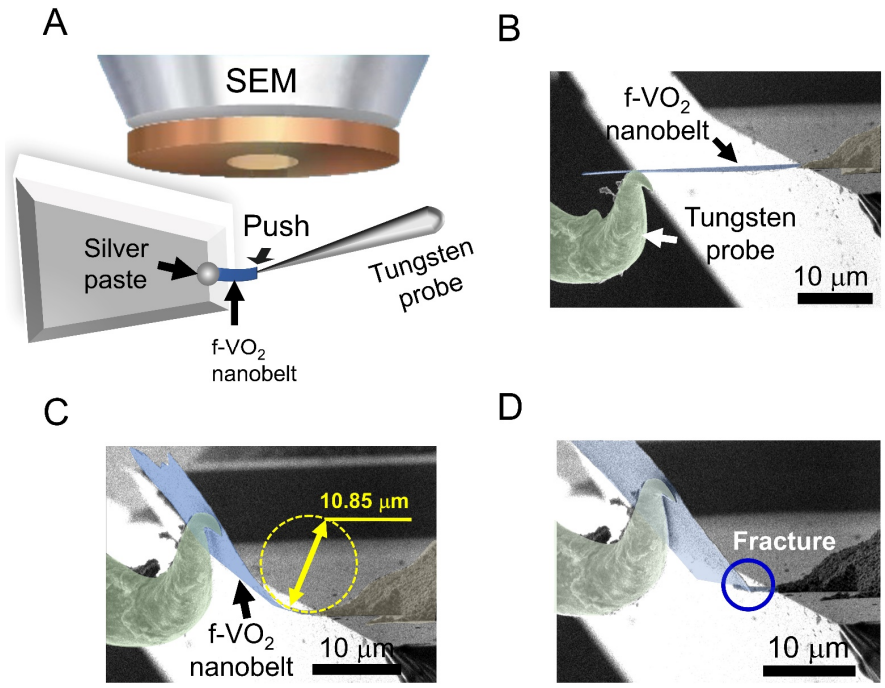

Fig. S11 Measurement of the mechanical property of the f-VO_2 film. (**A**) Schematic diagram for *in-situ* bending of the f-VO_2 film in the SEM using the tungsten probe. (**B**) SEM image showing the tungsten probe touch the f-VO_2 nanobelt. (**C**) Bending the f-VO_2 nanobelt to curvature of 0.184 μm^{-1}. (**D**) SEM image for the fracture of the f-VO_2 nanobelt.

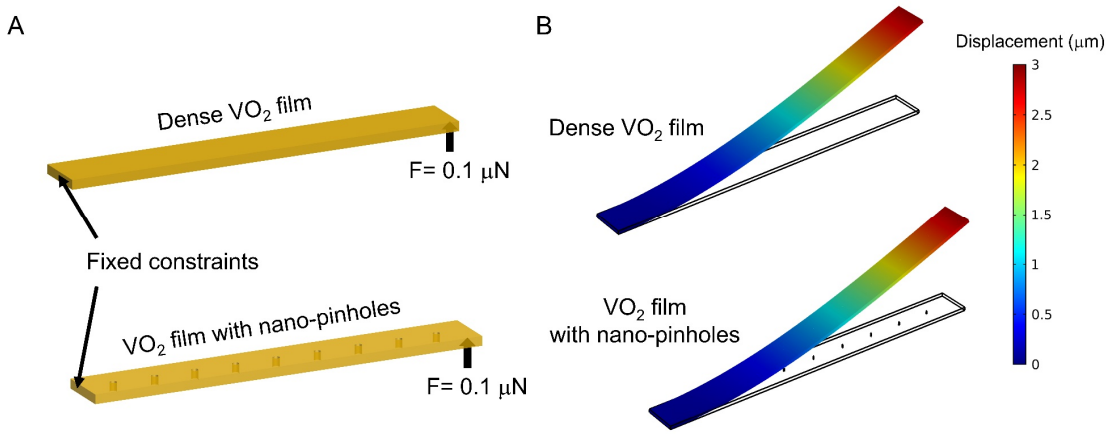

Fig. S12 Simulation of mechanical deformations of VO_2 films. (**A**) Geometrical models of the dense VO_2 film and the VO_2 film with nano-pinholes. (**B**) Deformations of the dense VO_2 film and the VO_2 film with nano-pinholes pushed by force.

Deformations of the dense VO_2 film and the VO_2 film with nano-pinholes pushed by force were simulated by the solid mechanics model in COMSOL Multiphysics software. For the solid mechanics model, the equation $\nabla \cdot S + F_v = 0$ was solved, where S was the stress tensor and F_v was the deformation gradient. In our simulation, the length, width, and thickness of the VO_2 film were 10, 1, and 0.1 μm, respectively. For the VO_2 film with nano-pinholes, the diameter of a nano-pinhole and the interval space between nano-pinholes were 20 nm and 1 μm, respectively. The Young's modulus of the VO_2 film was set to be 140 Gpa.

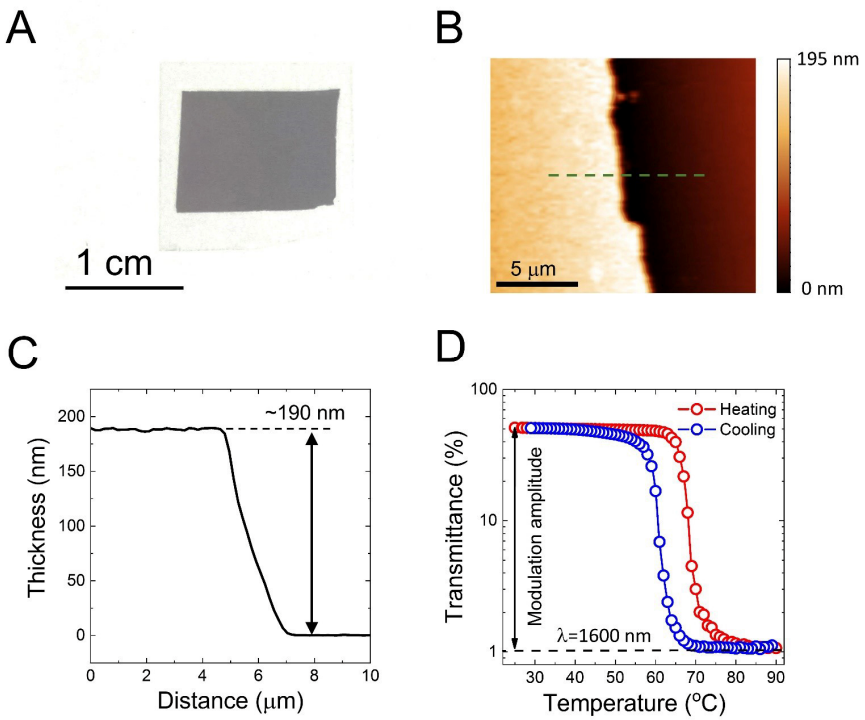

Fig. S13 Optical property of the f-VO_2/mica film. (**A**) Optical image of the f-VO_2/mica film. Photo credit: He Ma, Beijing University of Technology. (**B**) AFM image at the edge of the VO_2 film. (**C**) Height profile along the dashed line in Fig. S13B, indicating the thickness of the VO_2 film is ~190 nm. (**D**) Temperature-dependent transmittance of the f-VO_2/mica film at the wavelength of 1600 nm.

The transmittance of the f-VO_2/mica film is 51.08% at room temperature and decreases to 1.07% at 90 °C. the modulation amplitude of the f-VO_2/mica film attains 50.1% at the wavelength of 1600 nm.

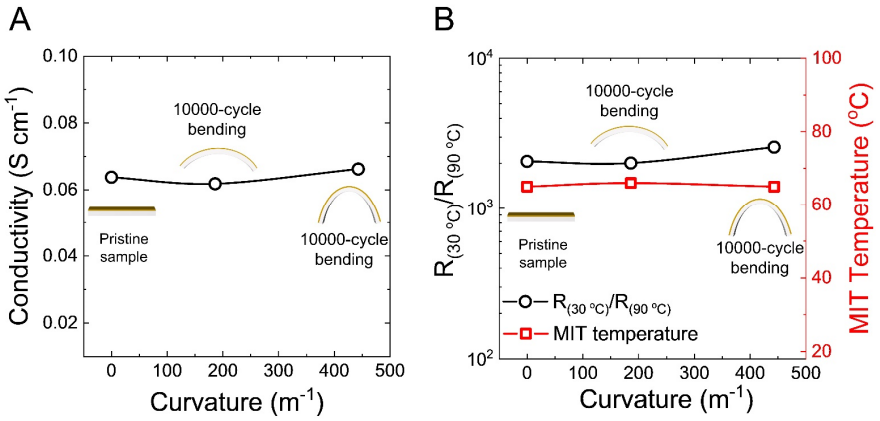

Fig. S14 Dependence of electrical properties of f-VO_2/mica films on the curvature and the bending cycles. (**A**) Electrical conductivity of f-VO_2/mica films as a function of curvature. (**B**) Resistance change ratio from 30 to 90 °C and MIT temperature (extracted from the heating curves) of the f-VO_2/mica films as a function of curvature.

We transferred an f-VO_2 film to a thin mica film and subsequently cut the VO_2/mica film into three pieces. The R-T relationship of sample #1 was measured directly, while those of samples #2 and #3 were measured after the samples were bent to the curvature of 186 and 443 m^{-1}, respectively, by 10,000 cycles. As shown in Fig. S14, the electrical conductivity, the resistance change ratio from 30 to 90 °C, and the MIT temperature of the VO_2/mica film are not altered with the curvature and bending cycles, demonstrating the excellent mechanical stability of the f-VO_2 film.

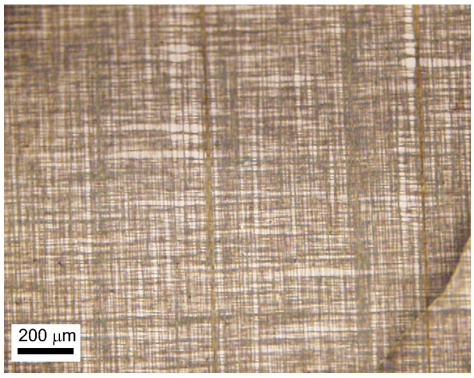

Fig. S15 Optical microscopy image of the f-VO_2/CNT film.

Table S3 Comparison of the THz modulation depth of different VO_2 films.

Sample	Thickness of VO_2 layer (nm)	Preparation method	Modulation depth	References
VO_2/Si	220	Sol-Gel	81%	(*63*)
VO_2/Quartz	190	Sol-Gel	84.2%	(*64*)
VO_2/SiO_2/Si	200	Sputtering	40%	(*65*)
VO_2/SiO_2/Si	210	Sputtering	67%	(*66*)
Nb-doping VO_2/SiO_2/Si	300	Sputtering	62.5%	(*67*)
Si-doping VO_2/SiO_2/Si	260	Sputtering	82%	(*68*)
VO_2/Diamond	120	Pulsed laser deposition	70%	(*69*)
VO_2/Sapphire	120	Sputtering	83%	(*70*)
VO_2/Sapphire	100	Pulsed laser deposition	86.7%	(*71*)
Van der Waals epitaxial VO_2/Mica film	192	Pulsed laser deposition	81.2%	(*72*)
Epitaxial VO_2 on c-plane sapphire	150	Sputtering	85%	(*73*)
f-VO_2/CNT film	**190**	**Sputtering**	**84%**	**This work**

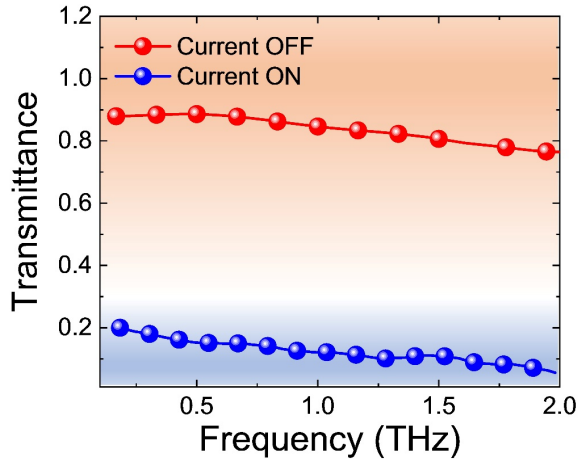

Fig. S16 Transmittance change of the f-VO_2/CNT film in the frequency range from 0.2 to 2 THz under electrical stimulation. The thickness of the f-VO_2 film is ~ 480 nm.

The modulation depth is defined as $(T_1-T_2)/T_1$, where T_1 and T_2 are transmittances without and with modulation. According to Fig. S16, for the 480-nm-thick f-VO_2 film, the maximum modulation depth of the f-VO_2/CNT film attains 94%.

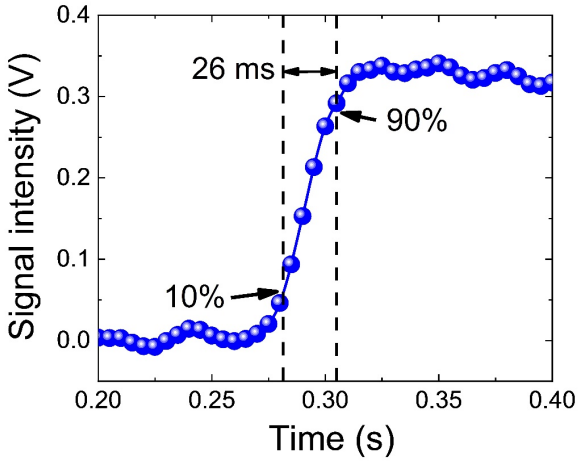

Fig. S17 Transient response of the THz modulator based on the f-VO_2/CNT film under electrical stimulation.

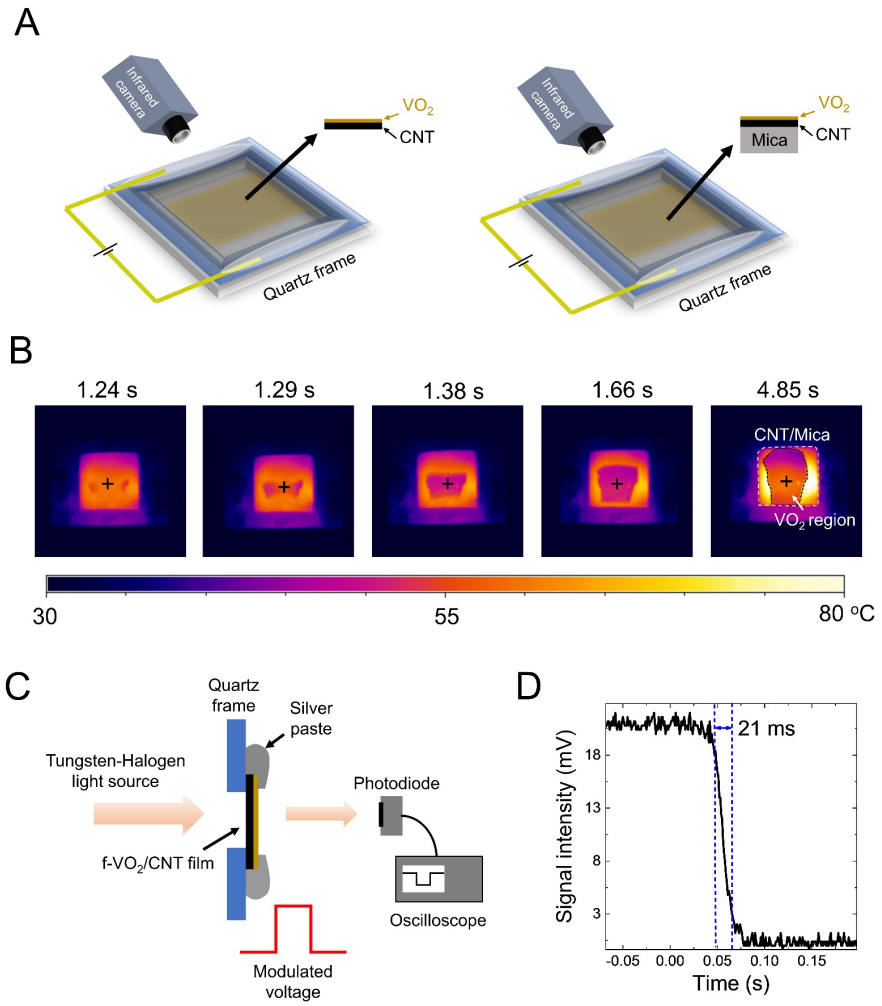

Fig. S18 Temperature changes of the f-VO_2/CNT film and the f-VO_2/CNT/mica film under electrical stimulation. (**A**) Schematic diagram for measuring nominal temperature changes of an f-VO_2/CNT film (left) and an f-VO_2/CNT/mica film (right) induced by Joule heating. (**B**) Thermograms of the f-VO_2/CNT/mica film from the time of 1.24 to 4.85 s in Fig. 3E. (**C**) Schematic diagram for measuring the transmittance change of the f-VO_2/CNT film under a square-wave modulated voltage. (**D**) Response time of the f-VO_2/CNT film under electrical stimulation.

We suspended an f-VO_2/CNT film and an f-VO_2/CNT/mica film on quartz frames and then made silver paste electrodes on the films (Fig. S18A). The temperature changes of the films due to Joule heating were *in-situ* recorded by the thermographic camera. We note that in the time-response curve of the f-VO_2/CNT/mica film, a sudden drop of the nominal thermographic temperature (T_{IR}) appears at 1.29 s (Fig. 3E), which is mainly attributed to the decrease of the emissivity induced by the MIT of VO_2. After this point, T_{IR} decreases (Fig. S18B) but the actual temperature keeps increasing until the maximum temperature is achieved. We also note that this process should also occur in the f-VO_2/CNT film, which, however, cannot be recorded by the thermographic camera because the fast heating process goes beyond the response time limit of the camera. To measure the actual response time of the f-VO_2/CNT film, we used a photodiode to record the modulation speed of the transmittance signal of the f-VO_2/CNT film under electrical stimulation (Fig. S18C). As shown in Fig. S18D, the response time of the f-VO_2/CNT film is only

21 ms for the transmittance change due to the thermally induced MIT, indeed shorter than the response time limit of the thermographic camera.

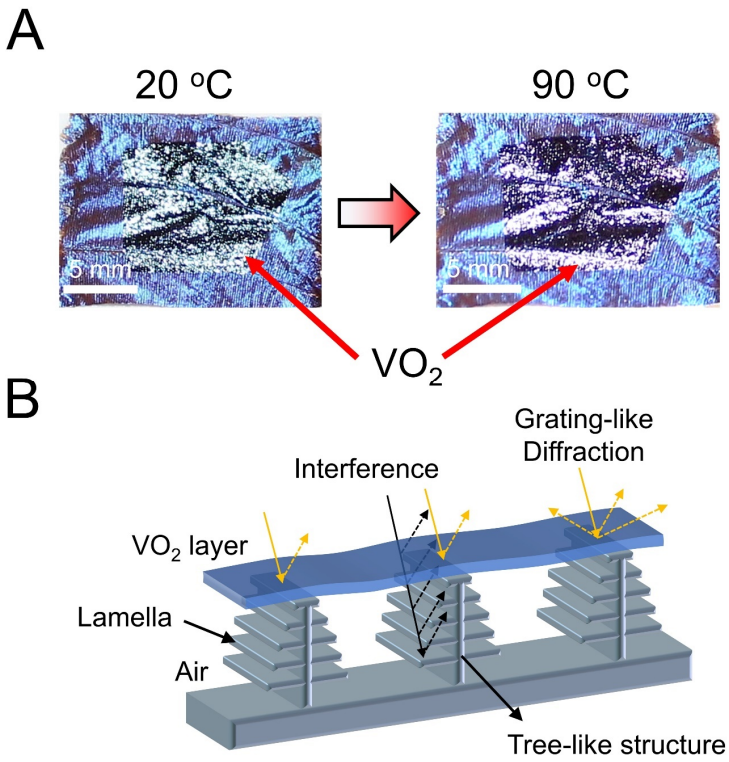

Fig. S19 Thermochromism of the VO_2-covered blue-morpho butterfly wing. (**A**) Photographs of a 120-nm-thick VO_2 film transferred to the surface of a butterfly wing, before (left, 20 °C) and after (right, 90 °C) heating. Photo credit: He Ma, Beijing University of Technology. (**B**) Schematic diagram for the structure color on the wing of the blue-morpho butterfly and the color tuning effects by covering a VO_2 film.

As shown in Fig. S19A, we observed dark green in the VO_2-covered region at 20 °C. The structure color changed to bright purple due to the MIT of VO_2 when the sample is heated to 90 °C. However, there is very little color change in the region of the pristine butterfly wing before and after heating.

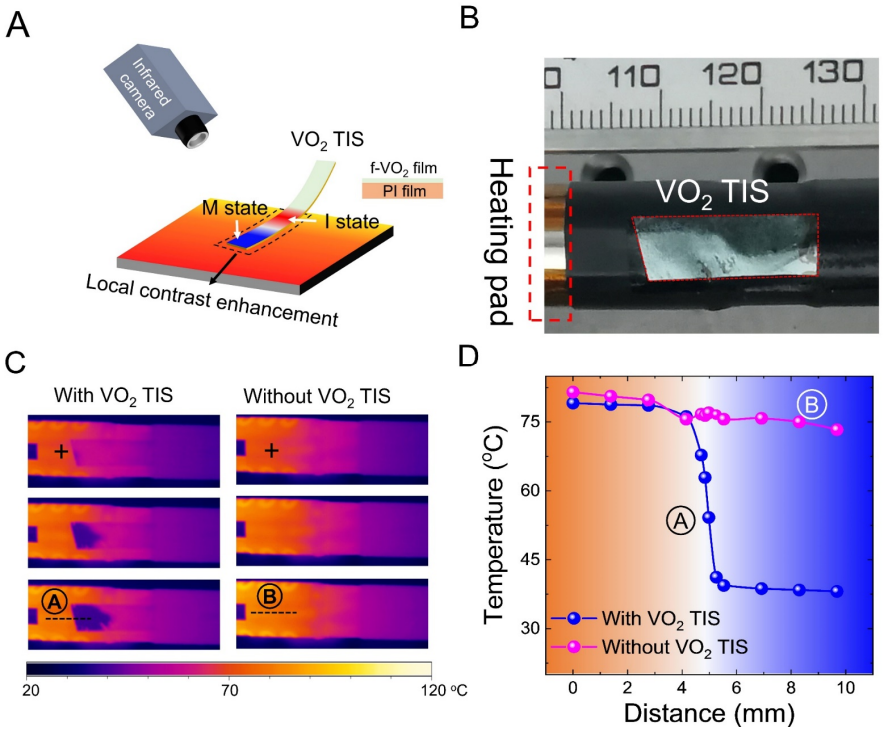

Fig. S20 Flexible temperature-indicating strip based on the f-VO_2/PI film. (**A**) Working principle of the VO_2 temperature-indicating strip (TIS). (**B**) Optical image of the VO_2 TIS attached to a metal pillar with a heating pad at one end. The bare surface of the metal pillar was covered with a high emissivity coating. Photo credit: He Ma, Beijing University of Technology. (**C**) Thermograms for the pillar with the VO_2 TIS and without the VO_2 TIS under heating. The temperature-monitor point was marked by the cross in the upper panel. The temperature of the monitor point in the upper, middle, and lower panels are 70, 75, and 80 ºC, respectively. (**D**) Temperature profiles along the dashed lines in Fig. S20C.

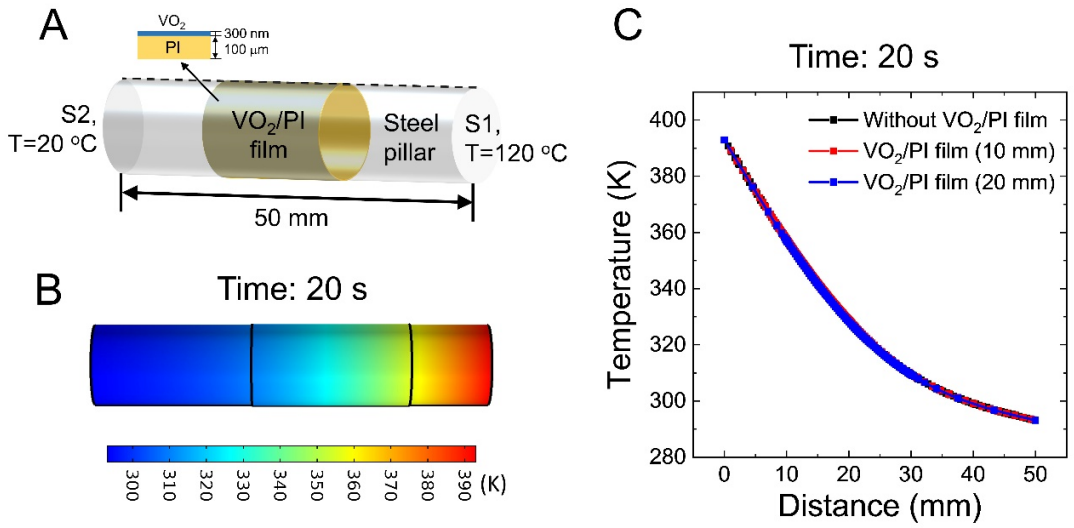

Fig. S21 Transient thermal-transfer simulation to the pillar covered with flexible VO_2 temperature-indicating strips. (**A**) Geometrical model of the pillar covered with a VO_2/PI film. (**B**) Temperature distribution on the surface of the pillar covered with the VO_2/PI film. (**C**) Temperature distribution along the dashed line in Fig. S21A.

To study the influence of the strip length of the VO_2 TIS on the measured temperature profiles, we performed a transient thermal transfer simulation by the finite element method using COMSOL software. As shown in Fig. S21A, the geometrical model includes a cylinder-like metal pillar surrounded by a VO_2/PI film. The length and diameter of the pillar are 50 and 13 mm, respectively. The length of the VO_2/PI surrounding film varies at 0, 10, and 20 mm. The material parameters used in the simulation, including thermal conductivity, thermal capacitance, density, are obtained from the material database of the COMSOL software. The simulation starts when the two ends (S1 and S2) are set at 120 and 20 °C, respectively, at 0 s. The temperature distribution is obtained at the simulation time ranging from 0 to 20 s.

Fig. S21B shows the temperature distribution on the surface of the pillar covered with the 20-mm-long VO_2/PI film at the simulation time of 20 s. The temperature gradually decreases from the end S1 to S2. We extracted the temperature profile on the surface of the pillar along the dashed line marked in Fig. S21A and compared the temperature profiles of the pristine pillar, the pillar covered with a 10-mm-long VO_2/PI film, and the pillar covered with a 20-mm-long VO_2/PI film (Fig. S21C). We can see that the length of the VO_2/PI film does not influence the temperature distribution on the pillar.

REFERENCES AND NOTES

1. B. Hu, Y. Ding, W. Chen, D. Kulkarni, Y. Shen, V. V. Tsukruk, Z. L. Wang, External-strain induced insulating phase transition in VO_2 nanobeam and its application as flexible strain sensor. *Adv. Mater.* **22**, 5134–5139 (2010).

2. H. Ma, J. Hou, X. Wang, J. Zhang, Z. Yuan, L. Xiao, Y. Wei, S. Fan, K. Jiang, K. Liu, Flexible, all-inorganic actuators based on vanadium dioxide and carbon nanotube bimorphs. *Nano Lett.* **17**, 421–428 (2017).

3. K. Liu, C. Cheng, J. Suh, R. Tang-Kong, D. Fu, S. Lee, J. Zhou, L. O. Chua, J. Wu, Powerful, multifunctional torsional micromuscles activated by phase transition. *Adv. Mater.* **26**, 1746–1750 (2014).

4. K. Liu, C. Cheng, Z. Cheng, K. Wang, R. Ramesh, J. Wu, Giant-amplitude, high-work density microactuators with phase transition activated nanolayer bimorphs. *Nano Lett.* **12**, 6302–6308 (2012).

5. L. Xiao, H. Ma, J. Liu, W. Zhao, Y. Jia, Q. Zhao, K. Liu, Y. Wu, Y. Wei, S. Fan, K. Jiang, Fast adaptive thermal camouflage based on flexible VO_2/Graphene/CNT thin films. *Nano Lett.* **15**, 8365–8370 (2015).

6. K. Liu, S. Lee, S. Yang, O. Delaire, J. Wu, Recent progresses on physics and applications of vanadium dioxide. *Mater. Today* **21**, 875–896 (2018).

7. S. Lee, K. Hippalgaonkar, F. Yang, J. Hong, C. Ko, J. Suh, K. Liu, K. Wang, J. J. Urban, X. Zhang, C. Dames, S. A. Hartnoll, O. Delaire, J. Wu, Anomalously low electronic thermal conductivity in metallic vanadium dioxide. *Science* **355**, 371–374 (2017).

8. Y. Ke, S. Wang, G. Liu, M. Li, T. J. White, Y. Long, Vanadium dioxide: The multistimuli responsive material and its applications. *Small* **14**, 1802025 (2018).

9. H. Ma, X. Xiao, X. Zhang, K. Liu, Recent advances for phase-transition materials for actuators. *J. Appl. Phys.* **128**, 101101 (2020).

10. Y. Guo, X. Sun, J. Jiang, B. Wang, X. Chen, X. Yin, W. Qi, L. Gao, L. Zhang, Z. Lu, R. Jia, S. Pendse, Y. Hu, Z. Chen, E. Wertz, D. Gall, J. Feng, T. M. Lu, J. Shi, A reconfigurable remotely epitaxial VO_2 electrical heterostructure. *Nano Lett.* **20**, 33–42 (2020).

11. W. Jiang, T. Zheng, B. Wu, H. Jiao, X. Wang, Y. Chen, X. Zhang, M. Peng, H. Wang, T. Lin, H. Shen, J. Ge, W. Hu, X. Xu, X. Meng, J. Chu, J. Wang, A versatile photodetector assisted by photovoltaic and bolometric effects. *Light Sci. Appl.* **9**, 160 (2020).

12. H. Luo, B. Wang, E. Wang, X. Wang, Y. Sun, Q. Li, S. Fan, C. Cheng, K. Liu, Phase-transition modulated, high-performance dual-mode photodetectors based on WSe_2/VO_2 heterojunctions. *Appl. Phys. Rev.* **6**, 041407 (2019).

13. B. Wang, R. Peng, X. Wang, Y. Yang, E. Wang, Z. Xin, Y. Sun, C. Li, Y. Wu, J. Wei, J. Sun, K. Liu, Ultrafast, kinetically limited, ambient synthesis of vanadium dioxides through laser direct writing on ultrathin chalcogenide matrix. *ACS Nano* **15**, 10502–10513 (2021).

14. J. Jiang, Z. Chen, Y. Hu, Y. Xiang, L. Zhang, Y. Wang, G. C. Wang, J. Shi, Flexo-photovoltaic effect in MoS_2. *Nat. Nanotechnol.* **16**, 894–901 (2021).

15. H. S. Kum, H. Lee, S. Kim, S. Lindemann, W. Kong, K. Qiao, P. Chen, J. Irwin, J. H. Lee, S. Xie, S. Subramanian, J. Shim, S. H. Bae, C. Choi, L. Ranno, S. Seo, S. Lee, J. Bauer, H. Li, K. Lee, J. A. Robinson, C. A. Ross, D. G. Schlom, M. S. Rzchowski, C. B. Eom, J. Kim, Heterogeneous integration of single-crystalline complex-oxide membranes. *Nature* **578**, 75–81 (2020).

16. L. Shen, L. Wu, Q. Sheng, C. Ma, Y. Zhang, L. Lu, J. Ma, J. Ma, J. Bian, Y. Yang, A. Chen, X. Lu, M. Liu, H. Wang, C. L. Jia, Epitaxial lift-off of centimeter-scaled spinel ferrite oxide thin films for flexible electronics. *Adv. Mater.* **29**, 1702411 (2017).

17. X. Li, Z. Yin, X. Zhang, Y. Wang, D. Wang, M. Gao, J. Meng, J. Wu, J. You, Epitaxial liftoff of wafer-scale VO_2 nanomembranes for flexible, ultrasensitive tactile sensors. *Adv. Mater. Technol.* **4**, 1800695 (2019).

18. K. Han, L. Wu, Y. Cao, H. Wang, C. Ye, K. Huang, M. Motapothula, H. Xing, X. Li, D. C. Qi, X. Li, X. R. Wang, Enhanced metal-insulator transition in freestanding VO_2 down to 5 nm thickness. *ACS Appl. Mater. Interfaces* **13**, 16688–16693 (2021).

19. Y. Chen, Z. Wang, S. Chen, H. Ren, L. Wang, G. Zhang, Y. Lu, J. Jiang, C. Zou, Y. Luo, Non-catalytic hydrogenation of VO_2 in acid solution. *Nat. Commun.* **9**, 818 (2018).

20. W. D. Kaplan, D. Chatain, P. Wynblatt, W. C. Carter, A review of wetting versus adsorption, complexions, and related phenomena: The rosetta stone of wetting. *J. Mater. Sci.* **48**, 5681–5717 (2013).

21. J. Y. Suh, R. Lopez, L. C. Feldman, R. F. Haglund Jr., Semiconductor to metal phase transition in the nucleation and growth of VO_2 nanoparticles and thin films. *J. Appl. Phys.* **96**, 1209–1213 (2004).

22. K. R. Williams, R. S. Muller, Etch rates for micromachining processing. *J. Microelectromech. Syst.* **5**, 256–269 (1996).

23. H. W. Chen, C. I. Li, C. H. Ma, Y. H. Chu, H. L. Liu, Strain engineering of optical properties in transparent VO_2/muscovite heterostructures. *Phys. Chem. Chem. Phys.* **23**, 8908–8915 (2021).

24. C. Cheng, K. Liu, B. Xiang, J. Suh, J. Wu, Ultra-long, free-standing, single-crystalline vanadium dioxide micro/nanowires grown by simple thermal evaporation. *Appl. Phys. Lett.* **100**, 103111 (2012).

25. J. Cao, E. Ertekin, V. Srinivasan, W. Fan, S. Huang, H. Zheng, J. W. Yim, D. R. Khanal, D. F. Ogletree, J. C. Grossman, J. Wu, Strain engineering and one-dimensional organization of metal-insulator domains in single-crystal vanadium dioxide beams. *Nat. Nanotechnol.* **4**, 732–737 (2009).

26. G. Zhou, P. Dai, J. Wu, B. Jin, Q. Wen, G. Zhu, Z. Shen, C. Zhang, L. Kang, W. Xu, J. Chen, P. Wu, Broadband and high modulation-depth THz modulator using low bias controlled VO_2-integrated metasurface. *Opt. Express* **25**, 17322–17328 (2017).

27. M. Seo, J. Kyoung, H. Park, S. Koo, H. S. Kim, H. Bernien, B. J. Kim, J. H. Choe, Y. H. Ahn, H. T. Kim, N. Park, Q. H. Park, K. Ahn, D. S. Kim, Active terahertz nanoantennas based on VO_2 phase transition. *Nano Lett.* **10**, 2064–2068 (2010).

28. H. Cai, S. Chen, C. Zou, Q. Huang, Y. Liu, X. Hu, Z. Fu, Y. Zhao, H. He, Y. Lu, Multifunctional hybrid metasurfaces for dynamic tuning of terahertz waves. *Adv. Opt. Mater.* **6**, 1800257 (2018).

29. F. Hu, Y. Li, X. Xu, Y. Zhou, Y. Chen, P. Zhu, S. Zhao, W. Jiang, W. Zhang, J. Han, Y. Chen, Broadband large-modulation-depth low-current-triggered terahertz intensity modulator based on VO_2 embedded hybrid metamaterials. *Appl. Phys. Express* **11**, 092004 (2018).

30. Y. G. Jeong, H. Bernien, J. S. Kyoung, H. R. Park, H. S. Kim, J. W. Choi, B. J. Kim, H. Kim, K. J. Ahn, D. S. Kim, Electrical control of terahertz nano antennas on VO_2 thin film. *Opt. Express* **19**, 21211–21215 (2011).

31. Z. Sun, A. Martinez, F. Wang, Optical modulators with 2D layered materials. *Nat. Photonics* **10**, 227–238 (2016).

32. C. Han, E. P. J. Parrott, G. Humbert, A. Crunteanu, E. Pickwell-MacPherson, Broadband modulation of terahertz waves through electrically driven hybrid bowtie antenna-VO_2 devices. *Sci. Rep.* **7**, 12725 (2017).

33. F. Fu, L. Shang, Z. Chen, Y. Yu, Y. Zhao, Bioinspired living structural color hydrogels. *Sci. Robot.* **3**, eaar8580 (2018).

34. X. Du, H. Cui, T. Xu, C. Huang, Y. Wang, Q. Zhao, Y. Xu, X. Wu, Reconfiguration, camouflage, and color-shifting for bioinspired adaptive hydrogel-based millirobots. *Adv. Funct. Mater.* **30**, 1909202 (2020).

35. H. Kim, H. Lee, I. Ha, J. Jung, P. Won, H. Cho, J. Yeo, S. Hong, S. Han, J. Kwon, K.-J. Cho, S. H. Ko, Biomimetic color changing anisotropic soft actuators with integrated metal nanowire percolation network transparent heaters for soft robotics. *Adv. Funct. Mater.* **28**, 1801847 (2018).

36. K. Tang, X. Wang, K. Dong, Y. Li, J. Li, B. Sun, X. Zhang, C. Dames, C. Qiu, J. Yao, J. Wu, A thermal radiation modulation platform by emissivity engineering with graded metal-insulator transition. *Adv. Mater.* **32**, 1907071 (2020).

37. K. Tang, K. Dong, C. J. Nicolai, Y. Li, J. Li, S. Lou, C.-W. Qiu, D. H. Raulet, J. Yao, J. Wu, Millikelvin-resolved ambient thermography. *Sci. Adv.* **6**, eabd8688 (2020).

38. M. Marezio, D. B. McWhan, J. P. Remeika, P. D. Dernier, Structural aspects of the metal-insulator transitions in Cr-doped VO_2. *Phys. Rev. B* **5**, 2541–2551 (1972).

39. X. Jin, H. Tan, Z. Wu, J. Liang, W. Miao, C. S. Lian, J. Wang, K. Liu, H. Wei, C. Feng, P. Liu, Y. Wei, Q. Li, J. Wang, L. Liu, X. Li, S. Fan, W. Duan, K. Jiang, Continuous, ultra-lightweight, and multipurpose super-aligned carbon nanotube tapes viable over a wide range of temperatures. *Nano Lett.* **19**, 6756–6764 (2019).

40. D. Lu, D. J. Baek, S. S. Hong, L. F. Kourkoutis, Y. Hikita, H. Y. Hwang, Synthesis of freestanding single-crystal perovskite films and heterostructures by etching of sacrificial water-soluble layers. *Nat. Mater.* **15**, 1255–1260 (2016).

41. Y. Zhang, L. Shen, M. Liu, X. Li, X. Lu, L. Lu, C. Ma, C. You, A. Chen, C. Huang, L. Chen, M. Alexe, C. L. Jia, Flexible quasi-two-dimensional $CoFe_2O_4$ epitaxial thin films for continuous strain tuning of magnetic properties. *ACS Nano* **11**, 8002–8009 (2017).

42. J. Qiao, S. Wang, Z. Wang, C. He, S. Zhao, X. Xiong, S. Wang, X. Zhang, X. Tao, Ultrasensitive and broadband all-optically controlled THz modulator based on $MoTe_2$/Si van der Waals heterostructure. *Adv. Opt. Mater.* **8**, 2000160 (2020).

43. Z. W. Shi, X. X. Cao, Q. Y. Wen, T. L. Wen, Q. H. Yang, Z. Chen, W. S. Shi, H. W. Zhang, Terahertz modulators based on silicon nanotip array. *Adv. Opt. Mater.* **6**, 1700620 (2018).

44. W. L. Chan, H. T. Chen, A. J. Taylor, I. Brener, M. J. Cich, D. M. Mittleman, A spatial light modulator for terahertz beams. *Appl. Phys. Lett.* **94**, 213511 (2009).

45. H. Ma, Y. Wang, R. Lu, F. Tan, Y. Fu, G. Wang, D. Wang, K. Liu, S. Fan, K. Jiang, X. Zhang, A flexible, multifunctional, active terahertz modulator with an ultra-low triggering threshold. *J. Mater. Chem. C* **8**, 10213–10220 (2020).

46. B. Sensale-Rodriguez, R. Yan, S. Rafique, M. Zhu, W. Li, X. Liang, D. Gundlach, V. Protasenko, M. M. Kelly, D. Jena, L. Liu, H. G. Xing, Extraordinary control of terahertz beam reflectance in graphene electro-absorption modulators. *Nano Lett.* **12**, 4518–4522 (2012).

47. S. Chen, F. Fan, Y. Miao, X. He, K. Zhang, S. Chang, Ultrasensitive terahertz modulation by silicon-grown MoS_2 nanosheets. *Nanoscale* **8**, 4713–4719 (2016).

48. H. T. Chen, W. J. Padilla, J. M. Zide, A. C. Gossard, A. J. Taylor, R. D. Averitt, Active terahertz metamaterial devices. *Nature* **444**, 597–600 (2006).

49. H.-T. Chen, W. J. Padilla, M. J. Cich, A. K. Azad, R. D. Averitt, A. J. Taylor, A metamaterial solid-state terahertz phase modulator. *Nat. Photonics* **3**, 148–151 (2009).

50. J. Kyoung, M. Seo, H. Park, S. Koo, H. S. Kim, Y. Park, B. J. Kim, K. Ahn, N. Park, H. T. Kim, D. S. Kim, Giant nonlinear response of terahertz nanoresonators on VO_2 thin film. *Opt. Express* **18**, 16452–16459 (2010).

51. Z. Fan, Z. Geng, X. Lv, Y. Su, Y. Yang, J. Liu, H. Chen, Optical controlled terahertz modulator based on tungsten disulfide nanosheet. *Sci. Rep.* **7**, 14828 (2017).

52. H. Kim, Y. Kim, K. S. Kim, H. Y. Jeong, A.-R. Jang, S. H. Han, D. H. Yoon, K. S. Suh, H. S. Shin, T. Y. Kim, W. S. Yang, Flexible thermochromic window based on hybridized VO_2/graphene. *ACS Nano* **7**, 5769–5776 (2013).

53. S. Bhupathi, S. Wang, M. Abutoama, I. Balin, L. Wang, P. G. Kazansky, Y. Long, I. Abdulhalim, Femtosecond laser-induced vanadium oxide metamaterial nanostructures and the study of optical response by experiments and numerical simulations. *ACS Appl. Mater. Interfaces* **12**, 41905–41918 (2020).

54. C. I. Li, J. C. Lin, H. J. Liu, M. W. Chu, H. W. Chen, C. H. Ma, C. Y. Tsai, H. W. Huang, H. J. Lin, H. L. Liu, P. W. Chiu, Y. H. Chu, Van der Waal epitaxy of flexible and transparent VO_2 film on muscovite. *Chem. Mater.* **28**, 3914–3919 (2016).

55. Y. Chen, L. Fan, Q. Fang, W. Xu, S. Chen, G. Zan, H. Ren, L. Song, C. Zou, Free-standing SWNTs/VO_2/Mica hierarchical films for high-performance thermochromic devices. *Nano Energy* **31**, 144–151 (2017).

56. T. Chang, Y. Zhu, J. Huang, H. Luo, P. Jin, X. Cao, Flexible VO_2 thermochromic films with narrow hysteresis loops. *Sol. Energ. Mat. Sol. C.* **219**, 110799 (2021).

57. H. Zong, H. Liu, L. Yan, Y. Yin, L. Bian, C. Kang, G. Cao, M. Li, Synchronized improvements of luminous transmittance and solar modulation ability of VO_2 films by employing SnO_2 buffer layers. *Thin Solid Films* **709**, 138174 (2020).

58. P. Zhang, W. Zhang, J. Wang, K. Jiang, J. Zhang, W. Li, J. Wu, Z. Hu, J. Chu, The electro-optic mechanism and infrared switching dynamic of the hybrid multilayer VO_2/Al:ZnO heterojunctions. *Sci. Rep.* **7**, 4425 (2017).

59. T. Kang, Z. Ma, J. Qin, Z. Peng, W. Yang, T. Huang, S. Xian, S. Xia, W. Yan, Y. Yang, Z. Sheng, J. Shen, C. Li, L. Deng, L. Bi, Large-scale, power-efficient Au/VO_2 active metasurfaces for ultrafast optical modulation. *Nanophotonics* **10**, 909–918 (2021).

60. G. Sun, X. Cao, X. Gao, S. Long, M. Liang, P. Jin, Structure and enhanced thermochromic performance of low-temperature fabricated VO_2/V_2O_3 thin film. *Appl. Phys. Lett.* **109**, 143903 (2016).

61. Z. Tian, B. Xu, B. Hsu, L. Stan, Z. Yang, Y. Mei, Reconfigurable vanadium dioxide nanomembranes and microtubes with controllable phase transition temperatures. *Nano Lett.* **18**, 3017–3023 (2018).

62. J. S. Sim, Y. Zhou, S. Ramanathan, Suspended sub-50 nm vanadium dioxide membrane transistors: fabrication and ionic liquid gating studies. *Nanoscale* **4**, 7056–7062 (2012).

63. Q. Shi, W. Huang, Y. Zhang, J. Yan, Y. Zhang, M. Mao, Y. Zhang, M. Tu, Giant phase transition properties at terahertz range in VO_2 films deposited by sol-gel method. *ACS Appl. Mater. Interfaces* **3**, 3523–3527 (2011).

64. H.-F. Zhu, L.-H. Du, J. Li, Q.-W. Shi, B. Peng, Z.-R. Li, W.-X. Huang, L.-G. Zhu, Near-perfect terahertz wave amplitude modulation enabled by impedance matching in VO_2 thin films. *Appl. Phys. Lett.* **112**, 081103 (2018).

65. S. Chen, H. Yuan, Z. Zhai, L. Du, S. Zhong, H. Zhu, Q. Shi, W. Huang, Z. Li, L. Zhu, All optically driven memory device for terahertz waves. *Opt. Lett.* **45**, 236–239 (2020).

66. X. Wu, Z. Wu, C. Ji, H. Zhang, Y. Su, Z. Huang, J. Gou, X. Wei, J. Wang, Y. Jiang, THz transmittance and electrical properties tuning across IMT in vanadium dioxide films by Al doping. *ACS Appl. Mater. Interfaces* **8**, 11842–11850 (2016).

67. C. Ji, Z. Wu, X. Wu, H. Feng, J. Wang, Z. Huang, H. Zhou, W. Yao, J. Gou, Y. Jiang, Optimization of metal-to-insulator phase transition properties in polycrystalline VO_2 films for terahertz modulation applications by doping. *J. Mater. Chem. C* **6**, 1722–1730 (2018).

68. H. Zhang, Z. Wu, R. Niu, X. Wu, Q. He, Y. Jiang, Metal–insulator transition properties of sputtered silicon-doped and un-doped vanadium dioxide films at terahertz range. *Appl. Surf. Sci.* **331**, 92–97 (2015).

69. A. Pashkin, C. Kübler, H. Ehrke, R. Lopez, A. Halabica, R. F. Haglund, R. Huber, A. Leitenstorfer, Ultrafast insulator-metal phase transition in VO_2 studied by multiterahertz spectroscopy. *Phys. Rev. B* **83**, 195120 (2011).

70. D. Fu, K. Liu, T. Tao, K. Lo, C. Cheng, B. Liu, R. Zhang, H. A. Bechtel, J. Wu, Comprehensive study of the metal-insulator transition in pulsed laser deposited epitaxial VO_2 thin films. *J. Appl. Phys.* **113**, 043707 (2013).

71. Z. Ren, L. Cheng, L. Hu, C. Liu, C. Jiang, S. Yang, Z. Ma, C. Zhou, H. Wang, X. Zhu, Y. Sun, Z. Sheng, Photoinduced broad-band tunable terahertz absorber based on a VO_2 thin film. *ACS Appl. Mater. Interfaces* **12**, 48811–48819 (2020).

72. W. Liang, Y. Jiang, J. Guo, N. Li, W. Qiu, H. Yang, Y. Ji, S. N. Luo, Van der Waals heteroepitaxial VO_2/Mica films with extremely low optical trigger threshold and large THz field modulation depth. *Adv. Opt. Mater.* **7**, 1900647 (2019).

73. C. Chen, Y. Zhu, Y. Zhao, J. H. Lee, H. Wang, A. Bernussi, M. Holtz, Z. Fan, VO_2 multidomain heteroepitaxial growth and terahertz transmission modulation. *Appl. Phys. Lett.* **97**, 211905 (2010).